Empirical study of an underwater optical camera communication system under turbulent conditions

Behnaz Majlesein,[1,*] Callum T. Geldard,[2] Victor Guerra,[3] Julio Rufo,[1,4] Wasiu O. Popoola,[2] and Jose Rabadan[5]

[1]*LightBee S.L., 35017 Las Palmas de Gran Canaria, Spain*
[2]*School of Engineering, Institute for Digital Communications, The University of Edinburgh, Edinburgh EH9 3JL, UK*
[3]*Pi Lighting Sarl, 1950, Sion, Switzerland*
[4]*Ramon y Cajal Researcher, Universidad de La Laguna (ULL), 38208 San Cristobal de La Laguna, Spain*
[5]*IDeTIC, Universidad de Las Palmas de Gran Canaria, 35017 Las Palmas de Gran Canaria, Spain*
[*]*bmajlesein@lightbeecorp.com*

Abstract: This paper presents an experimental study of the turbulence impact caused by temperature inhomogeneity and air bubbles on a global shutter-based underwater optical camera communication (UOCC). The effects of these two phenomena on UOCC links are illustrated in terms of the intensity variations and an associated reduction in the average received intensity of the illuminated pixels corresponding to the optical source projection and the dispersion of the projection on the captured images. Additionally, it is shown that the area of illuminated pixels in the temperature-induced turbulence scenario is higher than in the bubbly water case. To analyze the effects of those two phenomena on the optical link performance, the signal-to-noise ratio (SNR) of the system is evaluated by considering different points as the regions of interest (ROI) from the light source projection of the captured images. The results indicate that the system performance is improved by averaging over the value of several pixels produced by the point spread function, compared to simply using the central and the maximum pixel value as the ROIs.

1. Introduction

The demands for underwater wireless communication continue to grow with the expansion of marine exploration, scientific ocean observation, and ocean engineering [1]. Underwater optical wireless communication (UOWC) has attracted interest as a research topic in recent years, in part due to the fast propagation speed of light as well as the potential for high data rate transmission with low power consumption [2]. However, the reliability of such systems is highly affected by the absorption and scattering effects due to particles present in the seawater medium as well as underwater optical turbulence (UOT) [3]. UOT results from the random variation of the refractive index within the communication link caused by inhomogeneities in salinity, temperature, and air bubbles in the ocean. The mean density of the ocean depends on the depth, which increases as the temperature decreases. Bubbles are produced by breaking surface waves, the wake of ship propellers, and the release of different gasses from the seafloor, among other things [4]. UOT affects the propagation of optical signals by distorting their intensity, which may degrade the performance of the UOWC system [5]. Therefore, studying the channel effects is essential to developing a reliable UOWC system.

The effect of UOT has been experimentally evaluated in several works. In [6], the temperature-induced turbulence for the UOWC channel was modeled with a Log-Normal distribution under both weak and moderate turbulence regimes. Jamali et al. showed that two-lobe statistical

#491754 https://doi.org/10.1364/OE.491754
Received 28 Mar 2023; revised 11 May 2023; accepted 12 May 2023; published 12 Jun 2023

distribution, such as the mixed Exponential Log-Normal distribution, was required to model the effect of bubble-induced turbulence [7]. Moreover, it was illustrated that the received signal in the UOWC system might remain unaffected by salinity variations in a short-range link and stable water. The statistical channel model to characterize the turbulence caused by air bubbles, temperature, and salinity gradients was investigated in [8,9]. Qiu et al. proposed a comprehensive static model to characterize the turbulent underwater thermocline wireless optical channels induced by thermohaline gradient and air bubbles [10]. The proposed unified Weibull–Generalized Gamma distribution fitted well with the measured data under weak to strong turbulence regimes. In recent work, the composite UOWC channel model considering multiple scattering caused by particles and bubbles with different sizes was evaluated [11]. Geldard et al. studied the impact of turbulence-induced scattering on coherent light beams propagating in a water medium [12]. It was demonstrated that non-coherent light from a light-emitting diode (LED) source in a UOWC system had greater resilience to temperature inhomogeneity-induced turbulence than coherent light, transmitted by a laser source. Therefore, LEDs can be more suitable for UOWC in turbulent conditions, provided they meet the bandwidth requirements of the application. Moreover, the use of spatial diversity techniques in UOWC systems can mitigate the effect of turbulence and improve the system performance [13]. Different modulation schemes were compared in a turbulent condition for a UOWC link in [14]. The results confirmed that pulse position modulation (PPM) and subcarrier intensity modulation (SIM) are resilient to the effects of turbulence-induced fading.

As optical receivers, image sensors are potential candidates for alleviating the impact of the light beam angular fluctuations and optical attenuation taking advantage of their spatial diversity properties. Additionally, the spatial diversity offered by camera pixels provides the opportunity for spatial division multiplexing, as in [15]. Moreover, the performance degradation or link interruption caused by misalignment is reduced due to a larger field of view (FOV) compared to traditional UOWC receivers [16]. In recent years, underwater optical camera communication (UOCC) has been shown to be a promising technique for low data rate applications, as lots of underwater equipment is built with high-resolution image sensors for underwater exploration and research [17–21].

The complementary metal–oxide–semiconductor (CMOS) cameras can operate in both global-shutter (GS) and rolling-shutter (RS) modes. In GS mode, the entire sensor is exposed to the light at the same time, whereas in RS mode the image is generated row-by-row on the captured pixels [22]. Therefore, the data rate performance of the GS camera is limited to the frame rate of the camera due to capturing the single light source state in an image. In contrast, the RS camera has a higher data rate as multiple information bits are recovered within a single frame. However, the link distance can affect the achievable maximum throughput [23]. In the RS camera, the sampling rate is limited by exposure time (i.e. the time that the image sensor is exposed to the light), whereas, in the GS camera it does not affect the data rate but it allows more light to be integrated by the image sensor providing higher signal power as well as the noise level [24]. The GS camera is preferable in scenarios where achieving the longest link distance is more desirable than the data rate. In GS mode, if the area of projection is small or the link distance is long, the size of the projection area depending on the camera characterization in the image plane can theoretically be less than a single pixel considered a sub-pixel condition. Sub-pixel UOCC is a cost-effective and energy-efficient approach for some underwater wireless sensor network (UWSN) applications where many nodes and more extended data transmissions can be used. Tiny optical transmitters (e.g., micro LEDs) can be used in sub-pixel, where a large number of transmitters occupy a small area and take advantage of the camera spatial diversity to increase the throughput. However, some spatial energy dispersion due to scattering is created, producing a wider spot in the captured image even in a sub-pixel UOCC. This dispersion is modeled by a point spread function (PSF) of a system, describing the system spatial impulse response and is

dependent on the channel condition and link distance [25]. This effect can be more significant in an underwater environment where the impact of scattering is higher than in the air.

In this work, the system performance of a GS-based UOCC under turbulence conditions caused by bubbles and temperature inhomogeneity is experimentally investigated. This study evaluates the impact of these two phenomena on the UOCC system performance under different camera exposure times and identifies the fluctuations caused by turbulence-induced fading as significant challenges. As a communication link quality metric, the system SNR is measured considering different detection schemes for comparison. It is shown that using the average value of several illuminated pixels produced by PSF as the ROI can improve the system SNR by accounting for the energy spreading in the captured image due to the UOT-induced scattering effect in the UOCC channel. In addition, the heatmap of the illuminated pixels and tracking the maximum pixel value position over the course of data transmission is presented to demonstrate the impact of bubble and temperature inhomogeneity introduced on the energy distribution on the pixels into the ROI. The spread of pixels relates to a higher degree of spatial dispersion due to temperature-induced turbulence. Whereas, the maximum pixel value position placement in the bubbly condition implies deeper fading events than under temperature-induced turbulence. Moreover, the effect of these two phenomena on the received signal is illustrated. To the best of the author's knowledge, the effect of temperature inhomogeneity and bubble-induced turbulence on the UOCC and their impact on the received signal is studied for the first time in this paper, and the findings have important implications for improving the system performance under such conditions.

The rest of the paper is organized as follows: In Section 2, an overview of the UOCC system is discussed. Section 3 describes the methodology of the conducted experiments and setup. Section 4 is devoted to presenting the experimental results, and finally, the conclusion is drawn in Section 5.

2. Underwater optical camera communication

Multiple experiments using optical camera communication (OCC) in an underwater environment have been reported in the literature. In [17,18], a GS-based UOCC link performance analysis using multiple LED devices as transmitters in the link range of 1 m distance and the data rate of 100 bps and 750 bps, respectively, was achieved. In [19,20], the performance of an RS-based UOCC inside a tap, saline water, and the bubbly condition was studied. Their results demonstrated that the received signal in clear and salty water was approximately constant due to the low-range and stable underwater links. However, the bit error rate (BER) was corrupted under bubbly conditions due to heavy attenuation, distortion of the wavefront, and changing the direction of the propagating beam due to multiple scattering. Therefore, a de-bubble algorithm to combat bubble degradation was proposed to improve the system performance. Hamagami et al. evaluated and compared three different modulations, including phase-shift keying (PSK), non-return-to-zero on-off keying (NRZ-OOK), and orthogonal frequency division multiplexing (OFDM) in an RS-based UOCC system. Their results indicated that PSK could be the optimal modulation technique for RS-based UOCC systems due to more tolerance in an underwater environment in the presence of ambient light [26]. However, OOK modulation is an energy-efficient solution in a GS-based UOCC system with a low data rate due to the camera frame rate limitation [18]. In our recent work [21], the performance of GS-based UOCC under a sub-pixel condition is assessed. Accounting for this energy spreading due to the scattering effect of the UOCC channel, which causes an enlarged ROI mask and, as a result, improves the link SNR by considering the PSF as the desired ROI. However, the aforementioned studies have not investigated the effect of temperature inhomogeneity and bubbles-induced UOT on a GS-based UOCC system performance.

2.1. Turbulent UOCC link

In this section, (*i*) sub-pixel operation in a turbulent UOCC link is briefly described, (*ii*) the effect of temperature inhomogeneity and bubbles on light beam propagation and the received images are presented, and (*iii*) the scintillation index is defined.

As shown in Fig. 1, the size of the projection in the image plane depends on the camera configurations, image distance, sensor image dimensions, the target object size (i.e. the LED dimensions) and the camera distance with the object. In a regular camera operation, the projected area of the light source in the image affects a high number of pixels. However, if the link distance is large or the LED dimension is small, the captured image size can be less than a single pixel dimension theoretically, called the sub-pixel. To determine whether the dispersion effects mentioned above keep the system in a sub-pixel, it is necessary to measure the projection dimension in the image plane, which depends on the image distance of the camera. The image distance is derived by:

$$d' = \frac{S_{l,w}/2}{\tan(AOV_{H,V}/2)}, \tag{1}$$

where $S_{l,w}$ is the length or width of the image sensor, and $AOV_{H,V}$ is the horizontal or vertical camera angle of view. Therefore, the area of the projection in the image plane is:

$$\frac{l \times w}{d'^2} = \frac{L \times W}{d^2}, \tag{2}$$

where L, l and W, w are the length and width of the LED and its image, respectively and d is the link distance.

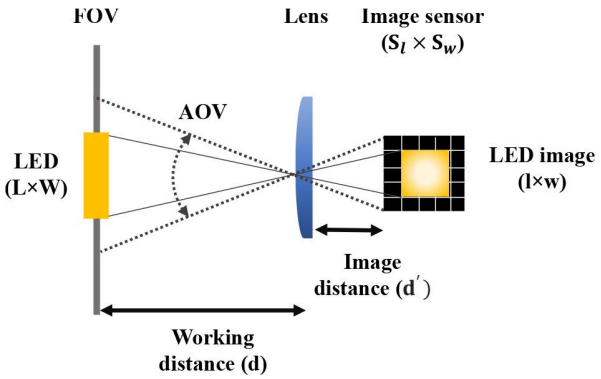

Fig. 1. Optical camera receiver structure and image acquisition in GS-based camera.

The light propagation in the water distributes the energy into more than one pixel due to the scattering effect. In Fig. 2(a), and 2(b), the effects of the bubble and temperature inhomogeneity on the spatial dispersion are illustrated, respectively. Due to the different refractive indices between the various interfaces generated by temperature changes or the presence of bubbles, the emitted light can experience single scattering, multiple scattering, and backscattering phenomena. Therefore, the area of the illuminated pixels evolves wider in the image plane. As it will be shown in the result section, this effect is higher in the bubbly and temperature inhomogeneous waters. In the bubbly water, the light beams pass through the air and water interfaces and scatter in different directions due to the random distribution of bubbles through the propagation path. In addition, since there is a more considerable difference in air and water refractive indices (i.e., $n = 1$ for air and $n = 1.33$ for pure water, respectively) compared to the refractive index caused by a temperature inhomogeneity, some of the light beams scatter at large deviation angles that

the receiver may not be able to capture as they are out of the receiver FOV, and they are lost. The angular distribution of intensity of the scattered light by an air bubble in water is given in [27]. Due to the interaction of the beam rays with bubbles of random sizes, some portion of the light beam may not reach the receiver. As a result, depending on the interaction of the beam with an air-water interface, the signal intensity varies in time and affects the received signal. When the bubble size is large enough, it completely blocks the beam thus causing a deep fading that causes a temporary communication disruption due to a severe drop in the channel. In addition, the frequency of the fluctuations is higher when the bubble population is higher, and the signal intensity fluctuations induced variance is significant because the intensity drops to zero at times [28].

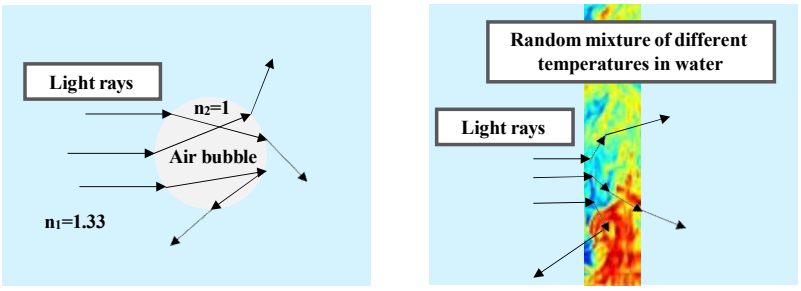

Fig. 2. (a) Bubble, and (b) temperature inhomogeneity effect on the light beam.

The strength of fluctuations in the received optical intensity, I, is described by the scintillation index, σ_I^2. This is defined as [29]:

$$\sigma_I^2 = \frac{\langle I^2 \rangle - \langle I \rangle^2}{\langle I \rangle^2}, \tag{3}$$

where $\langle\rangle$ is the mean operator. The scintillation index is used to distinguish between strong and weak turbulence in channel characterization. The turbulence is considered to be in the weak regime when $\sigma_I^2 < 1$.

3. Experiment methodology and setup

The main contribution of this work is to evaluate the system performance of a GS-based UOCC system under the temperature inhomogeneity and the presence of bubbles. The results focus on the impact of these two phenomena on the received signal and the communication performance. A block diagram of the experimental setup and decoding process is illustrated in Fig. 3. The optical emitter consists of an LED driven with NRZ Manchester-encoded OOK modulation signals. The optical beam propagates through an underwater channel emulator (UCE). The UCE consists of a large aquarium-style water tank in which the turbulent channel conditions can be controlled as in earlier work [12,14]. In this study, turbulence is generated in two ways: temperature inhomogeneity-induced turbulence, generated using a heating element positioned perpendicular to the propagating light beam in the center of the UCE; and bubble-induced turbulence, generated by injecting air into the bottom of the water tank through some aerator stones to create a continuous stream of bubbles through the path of the propagating light beam in the center of the UCE. This way, the levels of dispersion introduced by these two phenomena in the received signal can be compared experimentally. On the receiver side, a camera is used as the optical reception stage, capturing the images of the LED emissions. The received signal

is obtained after considering the ROI. Adaptive thresholding, taken as the mean value of the incoming signal packet is employed to sample the data and recover logic '1' and '0'. This approach can mitigate turbulence-induced fading effect [7]. After recovering the bit stream, the frame header is located in order to proceed with the packet reconstruction. Finally, the data is decoded, and the system performance is evaluated in terms of the SNR obtained for different camera exposure time configurations in clear water.

Figure 4 shows the experimental setup of the UOCC system under turbulent conditions caused by temperature inhomogeneity and bubbles. Python software is used as the platform for generating and decoding the data. Random data is generated by an arbitrary waveform generator. The structure of the UOCC data packet contains a 5-bit header and 10-bit payload. A bias tee is employed to drive the LED source for signal transmission. The system data rate is 5 bps which is limited by the frame rate in GS mode, and is suitable for certain applications within an Internet of underwater things (IoUT) network [21]. The transmitter (Tx) consists of a blue LED centered in 473 nm wavelength and transmission power of 67 μW. The optical signal is transmitted through a UCE filled with tap water with dimensions of 1.5 × 0.5 × 0.5 m^3. A Raspberry Pi Camera Module V2 (based on a Sony IMX219 sensor) on the receiver side is configured with a 1920 × 1080 pixels resolution and a frame rate of 30 fps. The Raspberry Pi Camera is employed in video capture mode, recording 3 minutes of videos for different camera exposure times of 50, 100, 200, 300, and 400 μs. The symbol duration is 6 times than 1/fps to assure that camera can capture at least one sample. In the demodulation part, the captured frames are extracted, and the ROI is selected. Different approaches are considered for obtaining the data signals selecting specific points as the ROI in the captured images, including the central point, the maximum intensity point, and an average value of 5×5 pixels around the central point in the projection of the source produced by the PSF on the captured image. After the above steps, the recovered data packet is examined for SNR calculation to evaluate the transmission performance of the UOCC system. The key system parameters are detailed in Table 1.

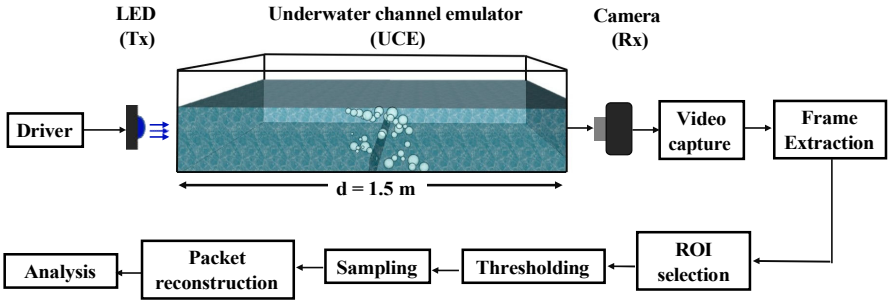

Fig. 3. Block diagram of the system setup and decoding process of the proposed GS-based UOCC.

The effects of air bubbles using an air pump with a stable air flow rate of around 4 liters per minute are introduced in the UCE via random size holes of a hose as illustrated in Fig. 5(a). The bubble size is random to simulate the real marine environment. A heat source controlled using an aquarium heater is employed for performing the turbulence generation within the link due to temperature inhomogeneity, as indicated in Fig. 5(b). A random mixture of different temperatures is created that causes turbulence-induced scattering, as in [14]. This way, a temperature inhomogeneity is created considering different temperature values along the UCE. The temperature is measured at four points, two in the center by the heat source and one by the Tx and Rx. The camera starts to record the video since the temperature difference within the

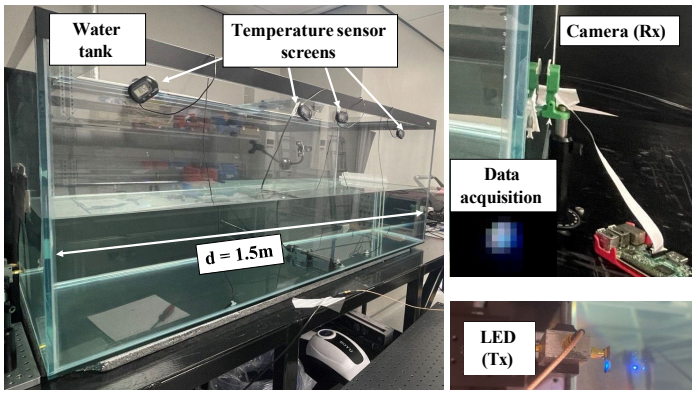

Fig. 4. Experimental setup in 1.5 m underwater channel, showing: LED (Tx), camera (Rx), a captured image, and underwater channel emulator equipped with temperature sensor screens.

Table 1. Key system parameters.

Parameter	Value
Transmitter	
LED	VLMB1500-GS08
Wavelength (nm)	473
LED diameter (mm)	1.0 × 0.5 (L × W)
Transmitted power (μW)	67
Received power (μW)	0.31
Modulation	NRZ-OOK
Data rate (bps)	5
Channel	
Water type	Tap water
Link distance (m)	1.5
Receiver	
Camera type	pi-camera V2 [30]
Camera resolution (px)	1920 x 1080
Image sensor diameter (mm)	2.15 x 1.2
Frame rate (fps)	30
Exposure time (μs)	50, 100, 200, 300, 400
Camera angle of view (AOV)	36.4 ˚(H), 21.4 ˚(V)
Optical power meter	Thorlabs-PM100

UCE between the temperature readings from the center and the two outer thermometers is around 5 degrees (ΔT=5 ˚C).

In this work, three-channel scenarios are considered: still water corresponds to the air pump and heater off (no inhomogeneity), temperature inhomogeneity-induced UOT corresponds to ΔT=5 ˚C, and bubble-induced UOT corresponds to air flow rate=4 L/min.

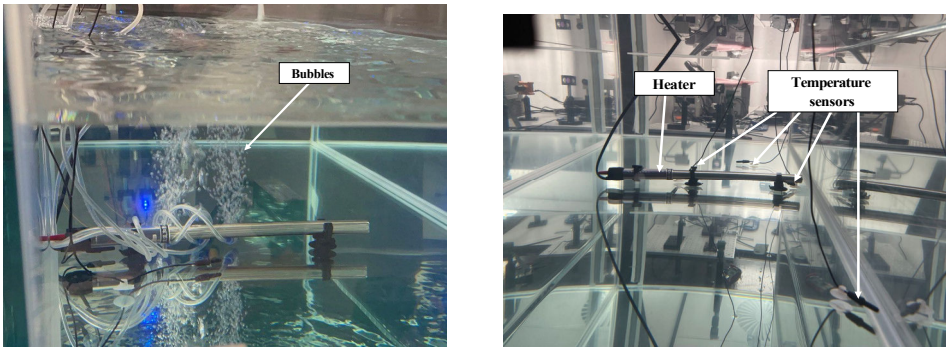

Fig. 5. Experimental setup used to study the effect of (a) bubble and (b) temperature inhomogeneity-induced turbulence underwater wireless optical channel: LED and camera.

4. Results

The performance of the GS-based UOCC system over a 1.5 m link distance in the presence of bubble and temperature inhomogeneity is discussed in this section. In this study, the transmission rate is very low, which means that the system is not limited by the bandwidth practically. Therefore, the "ON" pulses in the experiment are nearly rectangular in shape, and any variations in the received "ON" signal are only attributed to noise and/or turbulence. Furthermore, the OOK symbols are direct current (DC)-balanced. Consequently, there is no baseline DC wander in the system. Thus, any amplitude jitter from the OOK generator is negligible. As a result, the scintillation index using (3) is calculated by considering only the high received signal level values (i.e., only the signal values above a certain threshold) for the turbulent channel conditions. Moreover, the system SNR is used as a reference parameter to evaluate the communication system performance under different conditions (i.e., still, temperature inhomogeneity, and bubble-induced turbulence). To calculate the SNR, the average intensity and noise power of the received signal needs to be determined [16]. The amplitude of the incoming OOK signal determines the intensity of the received signal in the OCC system. The high received signal level values, i.e., only the signal values above a certain threshold are considered to calculate the average received intensity and noise variance since the low received signal level values are absolute zero due to the low camera exposure times. Therefore, the mean value and variance of high received signal level values are the average received signal intensity and noise power, respectively. The scintillation index and the system SNR are evaluated for the bubbly condition with the air flow rate of 4 L/min, and temperature inhomogeneity with ΔT=5 $^{\circ}$C considering all the illuminated pixels as the ROI and is shown in Fig. 6. It is demonstrated that the scintillation index with increasing the camera exposure times decreases while the system SNR improves in both bubbly and temperature inhomogeneity conditions. Although the scintillation index depends on channel conditions, increasing the camera exposure times cause more integrated power, which means that more signal energy is captured over a longer period of time. This can lead to a more stable signal with less variation and a lower scintillation index. The turbulence regime in the bubbly and temperature inhomogeneity conditions is weak, as the scintillation index is less than unity in both conditions in all the camera exposure times. In the following, the system SNR for different ROIs will be discussed in detail.

In order to indicate the light power distribution in the captured images and the impact of the bubbles and temperature inhomogeneity on them, the heatmaps for 100 µs exposure time of the illuminated pixels in the received images are presented in Fig. 7 and the distribution of the

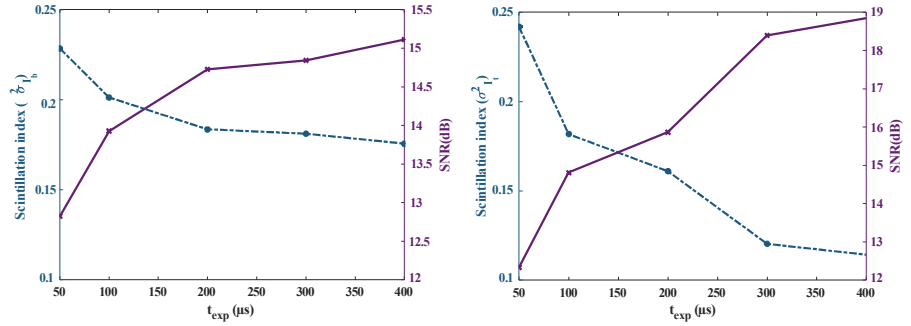

(a) Bubble (b) Temperature inhomogeneity

Fig. 6. Scintillation index and SNR against camera exposure times for two channel conditions: (a) bubble and (b) temperature inhomogeneity induced turbulence.

maximum-value pixel for each frame over the course of data transmission is shown in Fig. 8. The heatmap of tracking the maximum pixel value position over the course of data transmission indicates the impact of turbulence on deviating the beam from its original alignment and that the different sources of turbulence act in different ways. To create this; first, the maximum pixel value for each frame is identified, and its value and position are recorded. Then, this data is combined to create a single array that contains the total number of occurrences for each pixel position across all frames. It visualizes which pixel positions have the highest maximum values over the entire series of frames. It appears that the heatmap of the maximum pixel value position experiences more displacement in the temperature case.

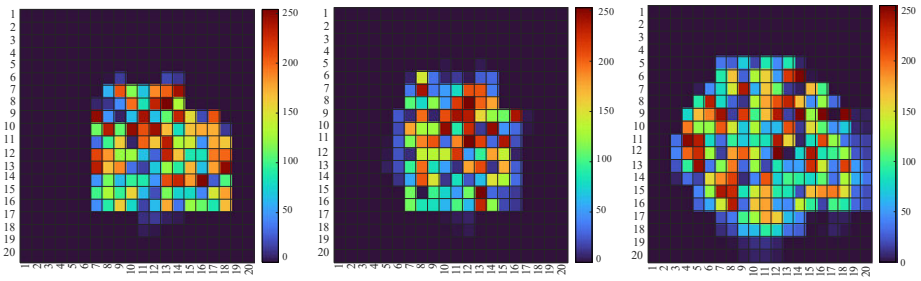

(a) Still (b) Bubbly (c) Temperature inhomogeneity

Fig. 7. Heatmap of illuminated pixels for three different channel conditions: (a) still, (b) bubbly, and (c) temperature inhomogeneity water.

The results illustrate that bubble and temperature inhomogeneity-induced UOT cause the propagating light beam dispersion. This effect is evidenced by the area of illuminated pixels and the enlarged source projection area in the captured images in Fig. 7(a), and 7(b) compared to that of still water in Fig. 7(b). Moreover, the dispersion effect is most significant in temperature-induced turbulence resulting in a greater spread of illuminated pixels. In the bubbly condition, since the refractive index of air bubbles and water interface is higher than temperature-induced refractive index variation, some light beams are out of the camera FOV and are not captured due to the multiple scattering and backscattering phenomena. Furthermore, the appearance of bubbles leads to severe fluctuations of light intensity due to the random distribution of bubbles through the propagation path, causing the light beams to randomly scatter in different directions and deviate from their original path. Another reason is that the size of the bubbles is large, which can be

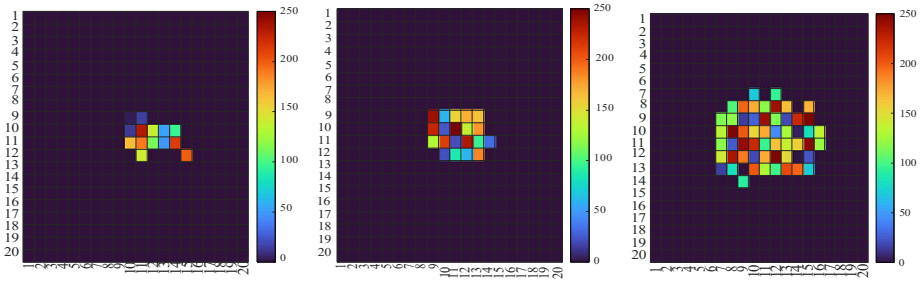

(a) Still (b) Bubbly (c) Temperature inhomogeneity

Fig. 8. Heatmap of tracking the maximum illuminated pixel value position over the course of data transmission for three different channel conditions (a) still, (b) bubbly, and (c) temperature inhomogeneity water.

considered an obstacle as mentioned in [10]. Therefore, the light intensity drops to zero due to the interaction with the large bubble, and the link may be blocked entirely at times. In a practical scenario, the dispersion effect would have an impact on the decoding of UOCC-encoded data where the received power intensity is not enough to detect, meaning bit '1' may be erroneously decoded as a bit '0'.

A pixel size in raspberry pi camera Module v2 is 1.12 × 1.12 μm^2. The image dimension of the transmitter LED size of 1 × 0.5 mm^2 in the image plane at the link distance of 1.5 m using (2) is 2.1 × 1.06 μm^2 considering the camera AOV and image sensor dimensions. Therefore, the system works theoretically under the sub-pixel condition in one dimension as the LED projection vertical dimension is less than the pixel one and in horizontal dimension is almost double. However, as shown in the heatmap plots, the captured illuminated pixels are much more than even two pixels due to the scattering effect of the water medium.

Figure 9 shows, by means of boxplot diagrams, the statistical properties of the received signal considering three different ROIs for five camera exposure times and in three different channel conditions, namely still (no inhomogeneity), bubbly (air flow rate= 4 L/min), and inhomogeneous temperature water (ΔT=5 ˚C). Figure 9(a) presents the measurements for still and turbulent water caused by temperature inhomogeneity and bubble for the single center pixel as the ROI. The results show that the average received power decreased in turbulent conditions, as expected. In the case of temperature inhomogeneity, the received power is lower and the standard deviation of the detected signal is higher than the bubble one. This is due to the higher scattering of the received image in the case of temperature, which causes the pixels with a higher intensity not to remain in the center of the image.

In Fig. 9(b), the maximum pixel is selected as the ROI, and a tracking process is performed in all the frames for the three-channel conditions and different camera exposure times under test. In contrast to the previous case, the average received power in the bubble-induced turbulence is less than in the temperature inhomogeneity condition and the standard deviation of temperature-induced turbulence is higher than the bubble. In this case, as the maximum value of the pixel is considered the ROI, the fading effect is lower in these points and the standard deviation in the bubble case is less than in the temperature-induced case. However, the bubble-induced UOT scattered the light more than the temperature case due to the higher difference in refractive indices between water and air interfaces, causing higher attenuation.

The average received power of both the bubbles and temperature-induced turbulence considering PSF (i.e. the average value of the 5×5 pixels around the central pixel) as the ROI is almost equal, as shown in Fig. 9(c). Therefore, considering several points reduce the signal variation compared to only one point, introducing averaging that can mitigate the impact of noise or variations in the

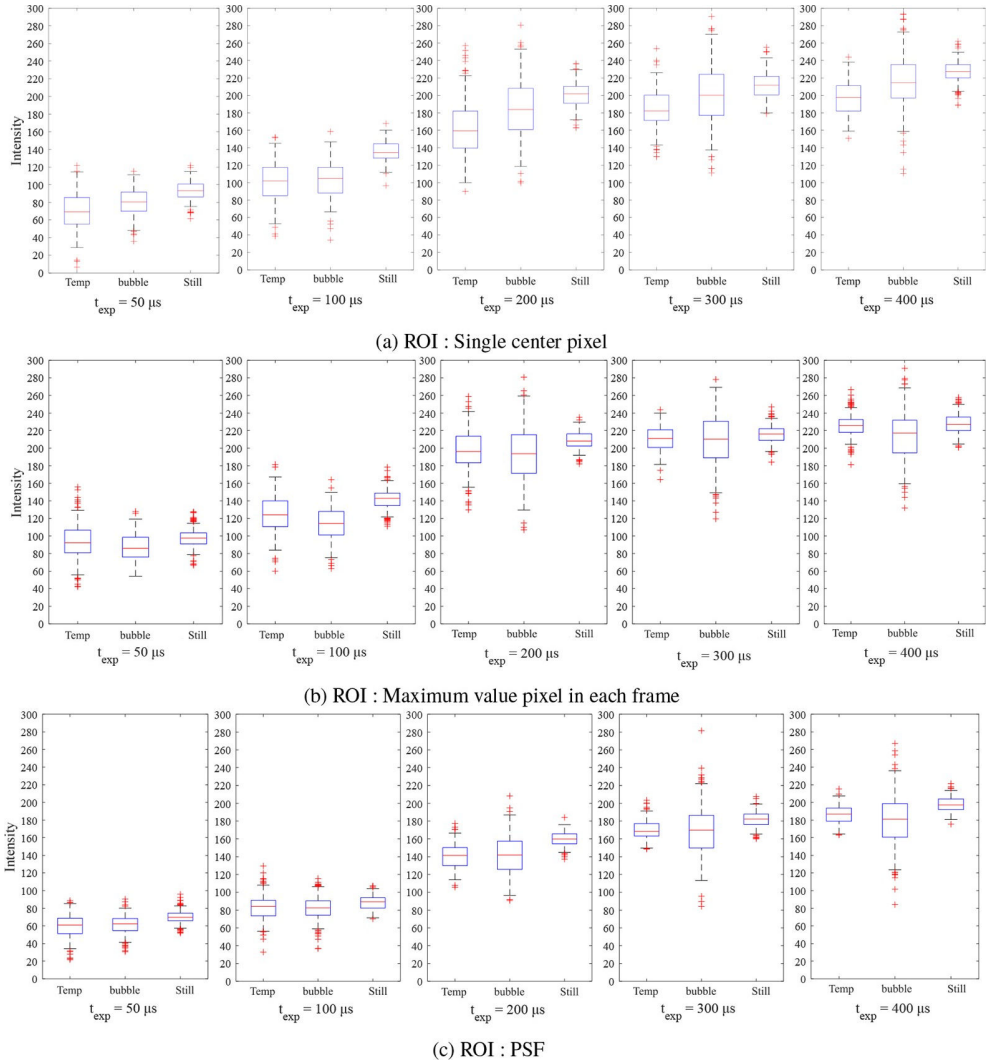

Fig. 9. Boxplots corresponding to three different channel conditions for different camera exposure times of 50, 100, 200, 300, and 400 µs considering (a) single center pixel,(b) tracking the maximum value in all the frames and (c) the PSF as the ROI.

final signals. The use of the PSF as the ROI can result in a lower average received signal and standard deviation than considering the single center pixel and the maximum value as the ROIs.

In general, as shown in all the cases of Fig. 9, the mean received signal and the standard deviation increase with increasing exposure time as the camera integrated more lights as well as noise. Some pixels are saturated for the still and inhomogeneous temperature water above the camera exposure time of 200 µs. Therefore, the exposure time above this value prevents the correct estimation of SNR at these points. However, the figures are demonstrated in all the exposure time values to compare the results with the bubbly conditions.

Figure 10 shows the evaluated SNR for 5-level exposure times in still and turbulent water for five different ROIs (i.e. the center pixel, the maximum pixel value of each frame, PSF, top and bottom pixel around the center pixel). The results show that the measured SNR in still water

considering the center, PSF, and the maximum pixel value of each frame is almost the same due to the absence of impurities to produce higher scattering. In addition, as the LED is aligned with the camera, the center pixel coincides with the maximum intensity pixel. The SNR improves by increasing the camera exposure time due to capturing more optical power. Considering air bubbles and temperature inhomogeneity effects, the system SNR reduces compared to still water. However, it is evident that the system SNR in both graphs considering the PSF as an ROI improves due to averaging out the variations in the received signal that can alleviate the noise impact. In the presence of air bubbles, by increasing the camera exposure time, the system SNR is not improved significantly due to the scattering. This is due to pixel intensity variation in time produced by the interaction between light and bubbles. Therefore, the PSF as the ROI where the average area of 5×5 pixels around the central point is considered can reduce the signal variation compared to a single point. The system SNR of the top and bottom pixels (2 (H) × 2 (V) upper and lower pixels around the center pixel) is provided to indicate the presence of the transmitted signal throughout the transmitter in the image. However, the level reduction is so significant that the reception quality deteriorates drastically. The SNR for still water rises with increasing the camera exposure time. However, the received SNR of these pixels behaves randomly for air bubbles and temperature inhomogeneity due to turbulence-induced scattering. The results clearly show that bubble and temperature inhomogeneity-induced UOT affect both received power and noise power due to the scattering effect. In addition, the PSF as the ROI can decrease the effect of temperature and bubbles on the received signal by averaging the area of the illuminated pixel.

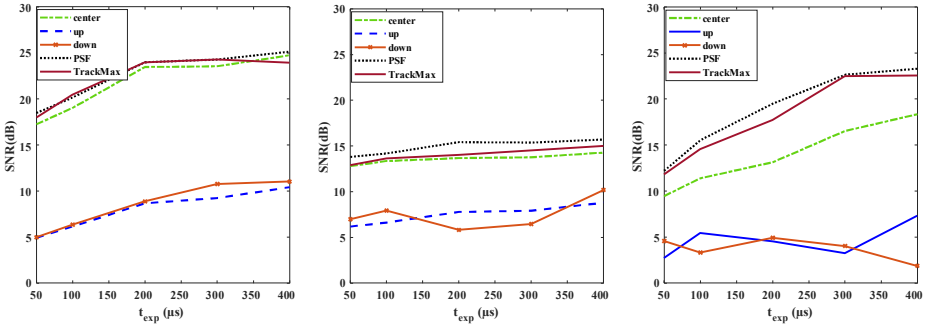

(a) Still (b) Bubbly (c) Temperature inhomogeneity

Fig. 10. SNR curve considering single center pixel, maximum tracked pixel, PSF, and top and bottom pixels under three different channel conditions: (a) still, (b) bubbly, and (c) temperature inhomogeneity water.

The received signal considering the PSF as the ROI for 100 μs exposure time in three-channel conditions is shown in Fig. 11, where the signal is more corrupted in the bubbly scenario. This shows the effect of temperature inhomogeneity and bubble-induced turbulence on UOCC. In the still water scenario, the received signal indicates stable intensity with a square shape, providing a clear distinction between '0' and '1' bits. Conversely, turbulence-induced fading causes the received signal to fluctuate over time making the distinction between bit levels less clear. Here, the shape of the received bit '1' pulses is no longer square as the channel coherence time is shorter than the symbol duration. This effect is most significant in the bubble-induced turbulence scenario, where the higher beam deviation angles lead to a greater likelihood of deep fades.

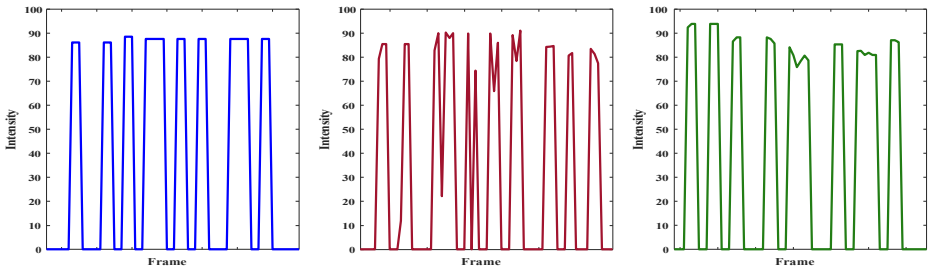

(a) Still (b) Bubbly (c) Temperature inhomogeneity

Fig. 11. Received signal considering PSF as the ROI for the camera exposure time of 100 μs under three different channel conditions: (a) still, (b) bubbly, and (c) temperature inhomogeneity water.

5. Conclusions

In this paper, the system performance of the GS-based UOCC for clear water under temperature inhomogeneity and bubble-induced UOT was studied empirically. The scintillation index was calculated in different camera exposure times for both turbulent conditions. It was shown that the system worked under a weak turbulent regime since the scintillation index was below unity in all camera exposure times. The results of heatmaps showed that the light energy was spread due to the scattering effect, causing an enlarged projection on the captured image. In addition, the temperature inhomogeneity-induced UOT caused more displacement of the maximum pixel value position over the course of data transmission, and also, the illuminated pixel area was higher than the bubble case. While bubbles caused multiple scattering and backscattering causing the loss of some light beams due to high beam deviation angles crossing the air-water interfaces. Moreover, the beam was blocked at times due to the significant size of the bubbles. The average received signal, and standard deviation were affected in both bubbly water and temperature inhomogeneity-induced UOT due to the scattering effect. The system SNR was measured to evaluate the system performance. The results demonstrated that temperature inhomogeneity and bubble-induced turbulence corrupted the system SNR. The experiments proved that accounting for the area of illuminated pixels produced by PSF due to the scattering effect as an ROI could improve the system SNR in turbulent conditions. Finally, the bubble and temperature inhomogeneity effect on the received signal was shown where the signals in the bubbly condition were more corrupted than the temperature inhomogeneity-induced turbulence.

Funding. Horizon 2020 Framework Programme (Marie Skłodowska Curie grant ENLIGHTEM No. 814215).

Acknowledgments. This work has been funded by the European Union's Horizon 2020 research and innovation programme under the Marie Skłodowska Curie grant agreement ENLIGHTEM No. 814215.

Disclosures. The authors declare no conflicts of interest.

Data availability. Data underlying the results presented in this paper are not publicly available at this time but may be obtained from the authors upon reasonable request.

References

1. N. Saeed, A. Celik, T. Y. Al-Naffouri, and M.-S. Alouini, "Underwater optical wireless communications, networking, and localization: A survey," Ad Hoc Networks **94**, 101935 (2019).
2. A. C. Boucouvalas, K. P. Peppas, K. Yiannopoulos, and Z. Ghassemlooy, "Underwater optical wireless communications with optical amplification and spatial diversity," IEEE Photonics Technol. Lett. **28**(22), 2613–2616 (2016).
3. Z. Zeng, S. Fu, H. Zhang, Y. Dong, and J. Cheng, "A survey of underwater optical wireless communications," IEEE Commun. Surv. Tutorials **19**(1), 204–238 (2017).
4. M. Singh, M. Lal Singh, R. Singh, H. Kaur, and P. Chohan, "Mitigation of turbulences induced by air bubbles and performance enhancement in 112 gbps uwoc link with coherent detection mimo pdm-qpsk and advanced digital signal processing," Opt. Quantum Electron. **54**(8), 472 (2022).

5. Y. Baykal, Y. Ata, and M. C. Gökçe, "Underwater turbulence, its effects on optical wireless communication and imaging: A review," Opt. Laser Technol. **156**, 108624 (2022).
6. Z. Vali, A. Gholami, Z. Ghassemlooy, M. Omoomi, and D. G. Michelson, "Experimental study of the turbulence effect on underwater optical wireless communications," Appl. Opt. **57**(28), 8314–8319 (2018).
7. M. V. Jamali, A. Mirani, A. Parsay, B. Abolhassani, P. Nabavi, A. Chizari, P. Khorramshahi, S. Abdollahramezani, and J. A. Salehi, "Statistical studies of fading in underwater wireless optical channels in the presence of air bubble, temperature, and salinity random variations," IEEE Trans. Commun. **66**, 4706–4723 (2018).
8. E. Zedini, H. M. Oubei, A. Kammoun, M. Hamdi, B. S. Ooi, and M.-S. Alouini, "Unified statistical channel model for turbulence-induced fading in underwater wireless optical communication systems," IEEE Trans. Commun. **67**(4), 2893–2907 (2019).
9. M. Singh, M. L. Singh, H. Kaur, H. Singh Gill, and S. Kaur, "Statistical channel model to characterize turbulence-induced fluctuations in the underwater wireless optical communication links," Int. J. Communication **35**(15), e5298 (2022).
10. H. Qiu, Z. Huang, J. Xu, W. Zhai, Y. Gao, and Y. Ji, "Unified statistical thermocline channel model for underwater wireless optical communication," Opt. Lett. **48**(3), 636–639 (2023).
11. L. Kou, J. Zhang, P. Zhang, Y. Yang, and F. He, "Composite channel modeling for underwater optical wireless communication and analysis of multiple scattering characteristics," Opt. Express **31**(7), 11320–11334 (2023).
12. C. T. Geldard, J. Thompson, and W. O. Popoola, "Empirical study of the underwater turbulence effect on non-coherent light," IEEE Photonics Technol. Lett. **32**(20), 1307–1310 (2020).
13. M. Singh, M. L. Singh, and R. Singh, "Performance enhancement of 112 gbps uwoc link by mitigating the air bubbles induced turbulence with coherent detection mimo dp-16qam and advanced digital signal processing," Optik **259**, 168986 (2022).
14. C. T. Geldard, E. Guler, A. Hamilton, and W. O. Popoola, "An empirical comparison of modulation schemes in turbulent underwater optical wireless communications," J. Lightwave Technol. **40**(7), 2000–2007 (2022).
15. C.-W. Chow, R.-J. Shiu, Y.-C. Liu, Y. Liu, and C.-H. Yeh, "Non-flickering 100 m rgb visible light communication transmission based on a cmos image sensor," Opt. Express **26**(6), 7079–7084 (2018).
16. N. Saeed, S. Guo, K.-H. Park, T. Y. Al-Naffouri, and M.-S. Alouini, "Optical camera communications: Survey, use cases, challenges, and future trends," Phys. Commun. **37**, 100900 (2019).
17. M. Akram, L. Aravinda, M. Munaweera, G. Godaliyadda, and M. Ekanayake, "Camera based visible light communication system for underwater applications," in *2017 IEEE International Conference on Industrial and Information Systems (ICIIS)*, (IEEE, 2017), pp. 1–6.
18. M. Akram, R. Godaliyadda, and P. Ekanayake, "Design and analysis of an optical camera communication system for underwater applications," IET Optoelectron. **14**(1), 10–21 (2020).
19. Z. Zhou, W. Guan, S. Wen, W. Xu, and Y. Li, "Rse-based underwater optical camera communication impeded by bubble degradation," in *Fourier Transform Spectroscopy*, (Optica Publishing Group, 2021), pp. JTu5A-8.
20. Z. Zhou, S. Wen, Y. Li, W. Xu, Z. Chen, and W. Guan, "Performance enhancement scheme for rse-based underwater optical camera communication using de-bubble algorithm and binary fringe correction," Electronics **10**(8), 950 (2021).
21. B. Majlesein, V. Matus, C. Jurado-Verdu, V. Guerra, J. Rabadan, and J. Rufo, "Experimental characterization of sub-pixel underwater optical camera communications," in *2022 13th International Symposium on Communication Systems, Networks and Digital Signal Processing (CSNDSP)*, (IEEE, 2022), pp. 150–155.
22. N.-T. Le and Y. M. Jang, "Mimo architecture for optical camera communications," The J. Korean Inst. Commun. Inf. Sci. **42**(1), 8–13 (2017).
23. N. T. Le, M. A. Hossain, and Y. M. Jang, "A survey of design and implementation for optical camera communication," Signal Process. Image Commun. **53**, 95–109 (2017).
24. O. I. Younus, N. B. Hassan, Z. Ghassemlooy, P. A. Haigh, S. Zvanovec, L. N. Alves, and H. Le Minh, "Data rate enhancement in optical camera communications using an artificial neural network equaliser," IEEE Access **8**, 42656–42665 (2020).
25. V. Matus, V. Guerra, C. Jurado-Verdu, S. Zvanovec, and R. Perez-Jimenez, "Wireless sensor networks using sub-pixel optical camera communications: Advances in experimental channel evaluation," Sensors **21**(8), 2739 (2021).
26. R. Hamagami, T. Ebihara, N. Wakatsuki, and K. Mizutani, "Optimal modulation technique for underwater visible light communication using rolling-shutter sensor," IEEE Access **9**, 146422–146436 (2021).
27. G. E. Davis, "Scattering of light by an air bubble in water," J. Opt. Soc. Am. **45**(7), 572–581 (1955).
28. H. M. Oubei, R. T. ElAfandy, K.-H. Park, T. K. Ng, M.-S. Alouini, and B. S. Ooi, "Performance evaluation of underwater wireless optical communications links in the presence of different air bubble populations," IEEE Photonics J. **9**(2), 1–9 (2017).
29. Y. Baykal, "Scintillations of led sources in oceanic turbulence," Appl. Opt. **55**(31), 8860–8863 (2016).
30. Sony Corporation, *IMX219PQH5-C, Diagonal 4.60 mm (Type 1/4.0) 8 Mega-Pixel CMOS Image Sensor with Square Pixel for Color Cameras, Datasheet* (Sony Corporation, 2014).